

Engineering Porous Carbon with Precise Sizes to Promote Surface-Dominated Storage in Sodium-Ion Batteries

Xin Lai,^[a] Xin Li,^[a] Qingquan Kong,^{*[a, b]} Xuguang An,^[a] Jing Zhang,^[a] Xiaolei Li,^[b] and Weitang Yao^{*[a, b]}

As the sole commercially viable anode material for sodium-ion batteries, hard carbon currently faces challenges such as slow diffusion kinetics in the low voltage range and low safety due to sodium deposition. In order to deepen the understanding of the pseudocapacitive processes of hard carbon in the high voltage range and enhance sodium storage capacity, this study systematically investigates the electrochemical performance and ion storage of ZIF-8-derived porous carbons (ZPCs) of different sizes. We propose a mathematical model based on a spherical particle core-shell structure, which profoundly reveals the relationship between size and specific surface area, as well as the linear relationship between specific surface area and

specific capacity. Moreover, simply by reducing the size of the porous carbon, the specific capacity increased by 86.5 mAhg⁻¹. Dynamic studies reveal that in nano-porous carbon materials, sodium-ion storage primarily relies on defect adsorption. Size reduction enhances physical adsorption and surface capacitance response, with ZPC-80 exhibiting lower resistance and higher diffusion coefficient, indicating that size reduction improves electronic conductivity and charge transfer efficiency, achieving excellent reversible capacity and cycling stability. This work yields a profound insight into the dynamic characteristics of hard carbon anode materials, presenting a new perspective for the design of efficient sodium-ion batteries.

1. Introduction

Due to the rapid development of renewable energy, alkali metal-ion batteries have been widely employed in energy storage applications such as consumer electronics, electric vehicles, and power grids.^[1] Among them, sodium-ion batteries (SIBs), based on abundant resources and cost-effective budgets, have gained significant attention for grid-scale energy storage applications.^[2] Compared to lithium-ion batteries, the significantly larger diameter of sodium ions (~1.02 Å) in comparison to Li⁺ (~0.76 Å) restricts their reversible storage capacity (~32 mAhg⁻¹) in commercial graphite anodes. The slow diffusion kinetics further limit the rate performance, posing significant challenges for the development and application of SIBs.^[3] Therefore, there is an urgent need to develop sodium-ion battery anode materials that combine high specific capacity and high rate performance.

In the past few years, notable advancements have been achieved both at home and abroad in the realm of negative electrode materials for SIBs, including embedded negative electrode materials such as hard carbon,^[4] metal oxides,^[5] conversion-type negative electrode materials like sulfides/^[6]

phosphides,^[6] and alloy-type negative electrode materials. Among them, hard carbon with a porous structure typically exhibits high sodium storage capacity and cycling stability.^[7]

For SIBs, the grain size, morphology, and crystallinity of the active material are critical factors determining its specific capacity, rate capability, and cycling stability.^[8] Reducing the grain size of the active material can effectively shorten the diffusion length, thereby enhancing the rate capability. Therefore, battery materials prepared at the nanoscale often exhibit significantly improved rate capability. For instance, Li et al. found that the sodium ion storage capacity significantly increased when the grain size reduced from 260 nm to 18 nm.^[9] Wei et al. identified that within TiO₂(A), the surface redox mechanism governing sodium ion storage is not constrained by semi-infinite diffusion, leading to outstanding rate capability, cycling stability, and reduced overpotential.^[10] However, there is limited research on the reaction mechanism and size effects of porous carbon in the high-voltage range pseudocapacitance. Therefore, it is essential to conduct a detailed dynamic analysis to investigate the size effects of porous carbon materials on the surface pseudocapacitive storage of sodium ions.

Porous carbon derived from MOFs in the realm of sodium-ion battery anodes, particularly ZIF-8, has gained prominence due to its high porosity and other advantageous properties. As early as 2015, Jing-Min Fan and colleagues prepared a composite material consisting of amorphous carbon nitride (ACN) and zinc oxide through thermal decomposition, thus establishing it as a promising candidate for sodium-ion battery anodes. Subsequently, ZIF-8 has found increasing applications in sodium-ion battery anodes.^[11] Qiya He employed ZIF-8 as a framework to construct a three-size columnar structure (ZIF-8-C@rGO) and discovered that the sodiumization products of ZIF-8 (NaZn₁₃, Na₂O, and nitrogen-doped carbon) exhibit a strong

[a] X. Lai, X. Li, Q. Kong, X. An, J. Zhang, W. Yao

School of Mechanical Engineering, Chengdu University, No. 2025, Chengluo Avenue, Chengdu 610106, P. R. China

[b] Q. Kong, X. Li, W. Yao

Interdisciplinary Materials Research Center, Institute for Advanced Study, Chengdu University, No. 2025, Chengluo Avenue, Chengdu 610106, Sichuan, China

E-mail: kongqingquan@cdu.edu.cn

yaoweitang@cdu.edu.cn

 Supporting information for this article is available on the WWW under <https://doi.org/10.1002/batt.202400129>

chemical affinity for sodium metal. This affinity induced favorable nucleation and guided the deposition of sodium. Furthermore, the columnar structure facilitated the diffusion of sodium ions within the graphene oxide sheets, promoting uniform current distribution and ensuring even deposition of sodium metal.^[12] Jiabao Li and colleagues successfully synthesized ZIF-8 with a unique polyhedral morphology and large size (approximately 2 μm) using a facile co-precipitation method. Following consecutive carbonization and sulfurization steps, they obtained ZnS nanoparticles decorated on nitrogen-doped porous carbon polyhedra (ZnS/NPC). When applied as a sodium-ion battery anode, ZnS/NPC exhibited a capacity of 370.6 mAh g^{-1} after 100 cycles at a rate of 0.1 A g^{-1} , and a capacity of 289.2 mAh g^{-1} after 1000 cycles at 1 A g^{-1} .^[13] Xingchen Xie and co-workers proposed a simple strategy to enhance sodium storage performance by in-situ growing MoSe₂ on nitrogen-doped porous carbon dodecahedra derived from zeolitic imidazolate framework-8 (ZIF-8). The nitrogen-doped porous carbon dodecahedra (N-PCD) provided a rapid electron transfer pathway for MoSe₂, and the robust interface between N-PCD and MoSe₂ alleviated structural changes in the electrode during sodium ion insertion/extraction.^[14] Despite the widespread application of ZIF-8 in sodium-ion battery anodes, there is currently a dearth of research articles that harness its inherent characteristics of regular shape, uniform pore size, and ease of particle size modulation to investigate the impact of size control on sodium-ion battery performance.

In this contribution, we successfully achieved precise control of the particle size of ZIF-8 derived porous carbon (ZPC) by adjusting the reactant concentration and further carbonization, thereby effectively enhancing the specific capacity of the sodium-ion battery anode. Through detailed dynamic analysis, we found that in nano-porous carbon materials, sodium ions primarily utilize defect adsorption as the main storage mechanism. The reversible specific capacity increases as the particle size decreases. From the micrometer to nanometer scale, the decrease in particle sizes results in an augmentation of the specific surface area, thereby enhancing the contact area of the large surface energy and reaction interface. In this context, we introduce a model for charge storage reliant on surface properties, meticulously delineating the correlation between particle size and specific surface area in porous materials, along with the linear association between specific capacity and specific surface area. This offers a quantitative examination of the relationship between size and capacity. The introduction of this model not only reveals the significance of size effects in porous materials but also provides crucial theoretical guidance for the design and optimization of high-performance porous anode materials to achieve outstanding sodium-ion battery performance.

Experimental

Synthesis of ZIF-8 Particles

Measure out 5.95 g (20 mmol) of $\text{Zn}(\text{NO}_3)_2 \cdot 6\text{H}_2\text{O}$ and 13.14 g (160 mmol) of 2-methylimidazole, and independently solubilize each in 200 mL of methanol, resulting in the formation of homogenous solutions. Subsequently, the 2-methylimidazole solution is gradually introduced into the $\text{Zn}(\text{NO}_3)_2 \cdot 6\text{H}_2\text{O}$ solution, followed by stirring at ambient temperature for a duration of 24 hours. Post-reaction, the resultant white precipitate is isolated via centrifugation, followed by multiple washes in methanol. The final step involves desiccating the sample under a vacuum at 60 °C for 12 hours. This study employed reactants with different moles, specifically 40 mmol and 60 mmol of $\text{Zn}(\text{NO}_3)_2 \cdot 6\text{H}_2\text{O}$. Under similar procedures, ZIF-8 precursors with varying diameters were obtained.

Synthesis of ZPC-Xs Materials

ZIF-8 powders of various diameters (200 mg) were subjected to thermal decomposition under an argon atmosphere at 1000 °C, with a ramping rate of 5 °C min⁻¹, and maintained in calcination for a period of 4 hours. This process yielded carbon materials of different diameters, namely ZPC-80, ZPC-470, and ZPC-910.

Materials Characterization

We employed the Bruker AXS D8 advance X-ray diffractometer with a scanning rate of 10 °C min⁻¹ to conduct a comprehensive investigation into the crystal structure of the materials. Raman spectroscopy data were obtained using the INVIA REFLEX (Renishaw) instrument, covering a wave number range of 150~4000 cm⁻¹, aimed at assessing the graphitization degree of the materials. X-ray photoelectron spectroscopy (XPS) analysis was carried out using the Thermo Fischer ESCALAB Xineneneea + instrument, with peak calibration referenced to the C1s peak at 284.8 eV, providing in-depth insights into the surface chemical properties of the materials. Additionally, we employed the Autosorb-Iq and Brunauer-Emmet-Teller (BET) methods to acquire nitrogen adsorption-desorption isotherms and pore size distribution data, enabling the exploration of the materials' pore characteristics and specific surface area. For surface morphology characterization of the materials, we utilized the FEI Insect F50 scanning electron microscope (SEM). Finally, the FEI Talos F200S Super transmission electron microscope (TEM) and energy-dispersive X-ray spectroscopy (EDS) were employed for high-resolution microscopic structural observations and elemental composition analysis.

Electrochemical Characterization

ZPC-Xs, Super P, and PVDF (employed as a binder) were combined in a ratio of 8:1:1 by mass and solubilized in N-methyl-2-pyrrolidone solvent to craft the negative electrode. The evenly distributed slurry was applied onto a copper foil current collector, underwent vacuum drying at 120 °C for 6 hours, and was subsequently punched to yield negative electrode discs with a diameter of 12 mm and a loading mass ranging from 1.2 to 1.6 mg cm⁻². Finally, the negative electrodes were integrated into coin cells (CR2032) within a glove box filled with high-purity argon gas, employing pure metallic sodium as the counter electrode. Whatman glass fiber was used as the separator, and the electrolyte comprised 1 mol L⁻¹ NaClO_4 dissolved in a solvent mixture of diethyl carbonate and ethylene carbonate (in a 1:1 v/v ratio). Continuous current charge-discharge experiments were conducted on the coin cells employing a battery testing system (Neware).

Cyclic voltammetry (CV) and electrochemical impedance spectroscopy (EIS) analyses were carried out on the negative electrode using an electrochemical workstation (CHI760 C, Shanghai Chenhua). The CV scan rate ranged from 0.1 to 5 mVs⁻¹, covering a voltage range of 0.01 to 3 V. EIS measurements were conducted with an amplitude of 5.0 mV and a frequency range of 0.01 to 10⁵ Hz.

2. Results and Discussion

Figure 1a illustrates a schematic diagram of the synthesis of ZPC with different sizes. In the synthesis of ZIF-8, particle size is determined by the rates of nucleation and growth.^[15] Factors such as the relative content of ligands and the concentration of the solution affect the size of ZIF-8 crystals.^[16] To effectively control the size of ZIF-8 and mitigate the potential impact of nitrogen content in 2-methylimidazole on battery performance, this experiment achieved precise control of solute content by fixing the ratio of Zn(NO₃)₂ to 2-methylimidazole and the

volume of methanol. High concentrations of reactants not only influence the rate of crystallization, thereby reducing the number of nuclei, but also promote crystal growth by affecting concentration gradients, leading to an increase in the final particle size.^[17] By adjusting the molar mass of Zn(NO₃)₂ to 20, 40, and 60 mmol, three different-sized ZIF-8 particles were successfully synthesized. Subsequently, the corresponding porous derived carbon materials were obtained through the carbonization process.

Scanning Electron Microscope (SEM) images illustrate that all samples exhibit a typical rhombic dodecahedron morphology (Figure 1b-d), with average diameters of 80, 470, and 910 nm (Figure S1-3), respectively named ZPC-80, ZPC-470, and ZPC-910. To verify the effect of carbonization temperature on particle size, 80 nm ZIF-8 was carbonized at 800 and 900 °C, as shown in Figure S4, with average diameters of 84 and 82 nm, respectively. This indicates that with the increase in carbonization temperature, there is a slight shrinkage in ZPC particles. However, compared to changing particle size by controlling reactant concentration, this shrinkage can be neglected. As

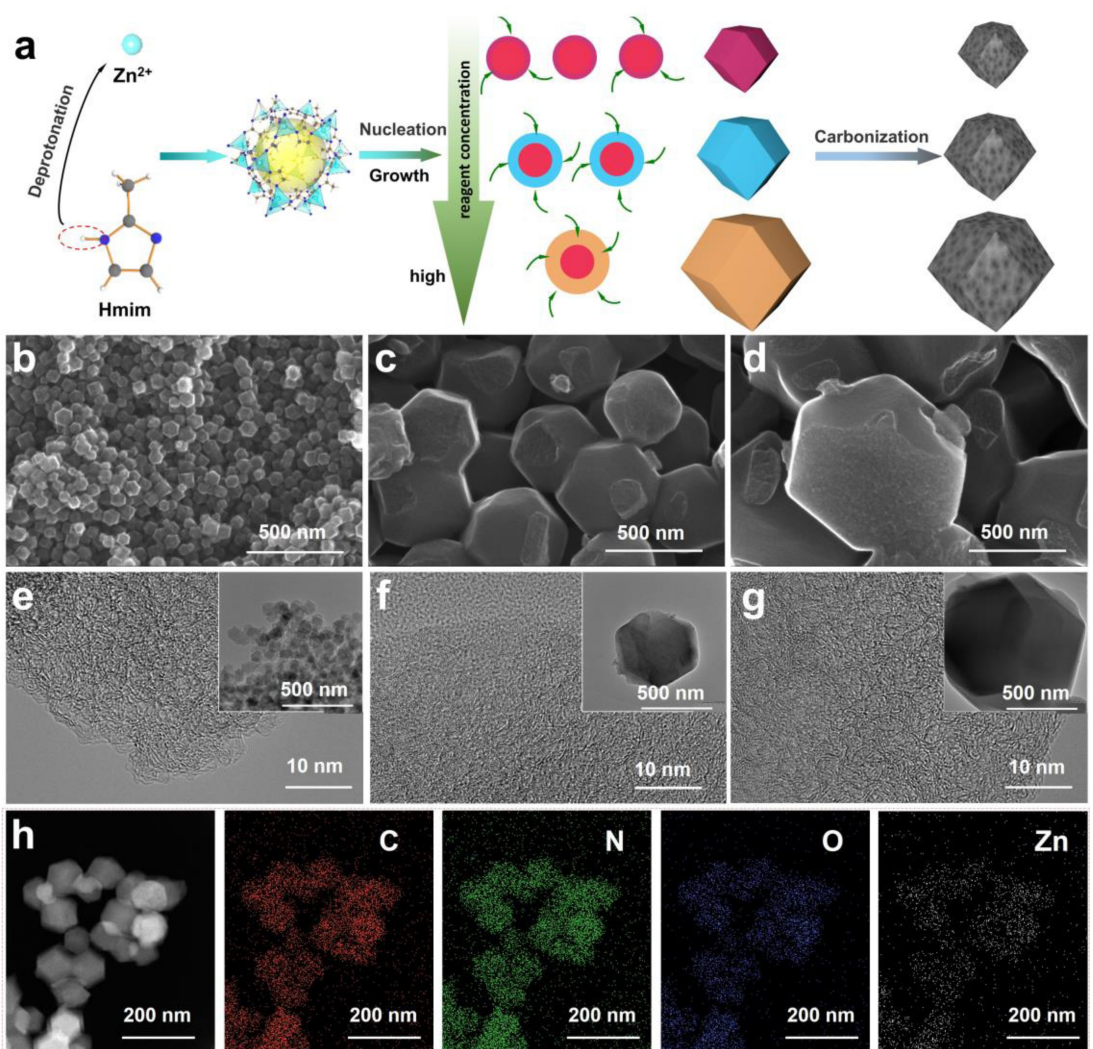


Figure 1. (a) Schematic illustration of ZPC powders synthetic procedures with controlled particle size. Morphology and structure characterization of ZPC powders. SEM images of (b) ZPC-80, (c) ZPC-470, and (d) ZPC-910. TEM images of (e) ZPC-80, (f) ZPC-470, and (g) ZPC-910. EDS mapping images of ZPC-80 (h).

shown in Figure 1e-g Transmission Electron Microscopy (TEM) analysis further confirmed the consistency in size, and the images showed the typical short-range ordered crystal microstructure of hard carbon. Energy spectrum analysis indicated that ZPC materials are mainly composed of C, N, O, and Zn elements, with carbon being the dominant element (Figure 1h).

X-ray Diffraction (XRD) analysis revealed the crystal structure characteristics of ZPC materials (Figure 2a). The XRD spectra of all samples exhibit typical peaks of amorphous carbon, without other peaks, indicating that most organic substances were decomposed during the heat treatment process.^[18] To further verify size control, we also conducted XRD analysis on the ZIF-8 precursor (Figure S5). The results align with the standard ZIF-8 pattern, and the intensity of the (011) peak at ~7.3° gradually increases with size, further confirming the success of size control.^[16]

N_2 adsorption/desorption experiments further examined the pore characteristics and specific surface area of these materials (Figure 2b). ZPC-80 shows a mixed type I/IV curve, with capillary condensation of N_2 at low pressures ($P/P_0 < 0.1$), indicating a predominantly microporous structure; the hysteresis loop at relative pressures $P/P_0 = 0.8$ and above is of type H3, indicating the presence of mesopores and irregular pore structure, likely due to particle agglomeration in ZPC-80.^[19] ZPC-470 and ZPC-910 primarily exhibit type I adsorption curves, indicating a microporous structure.^[20]

As the particle size increases, the specific surface area shows a decreasing trend, with corresponding specific surface areas of 1051.7, 963.3, and 958.8 $m^2 g^{-1}$, respectively (as depicted in Table S1). The micropore diameter distribution profiles acquired through the Barrett-Joyner-Halenda (BJH) technique revealed that the ZPC-Xs' pores were consistently concentrated at 0.67 nm (Figure 2b), thus substantiating the assumptions of the mathematical model presented below.

For the degree of graphitization of carbon materials, we conducted a detailed analysis through Raman spectroscopy. The Raman spectra were fitted with four Gaussian peaks at 1205, 1350, 1500, and 1590 cm^{-1} , and these peaks aligned with the T, D, D'', and G peaks, respectively (Figure 2c). The T peak represents the A_{1g} vibrational mode of sp^3 structure, while the D and D'' peaks correspond to defects in the stacking of graphene layers, and the G peak originates from the ordered graphite lattice. The defect density of carbon materials is typically expressed by the I_D/I_G value.^[21] From the graph, it can be observed that the I_D/I_G values are identical, both being 1.98, indicating similar defect densities and consistent surface disorder for these three samples.^[22]

The effect of nitrogen doping on ZPC in the negative electrode of sodium-ion batteries indeed involves multiple aspects. Firstly, nitrogen doping can alter the electronic structure and surface chemical properties of porous carbon particles, thereby affecting their conductivity and electrochemical activity.^[23] Different types of nitrogen doping, such as

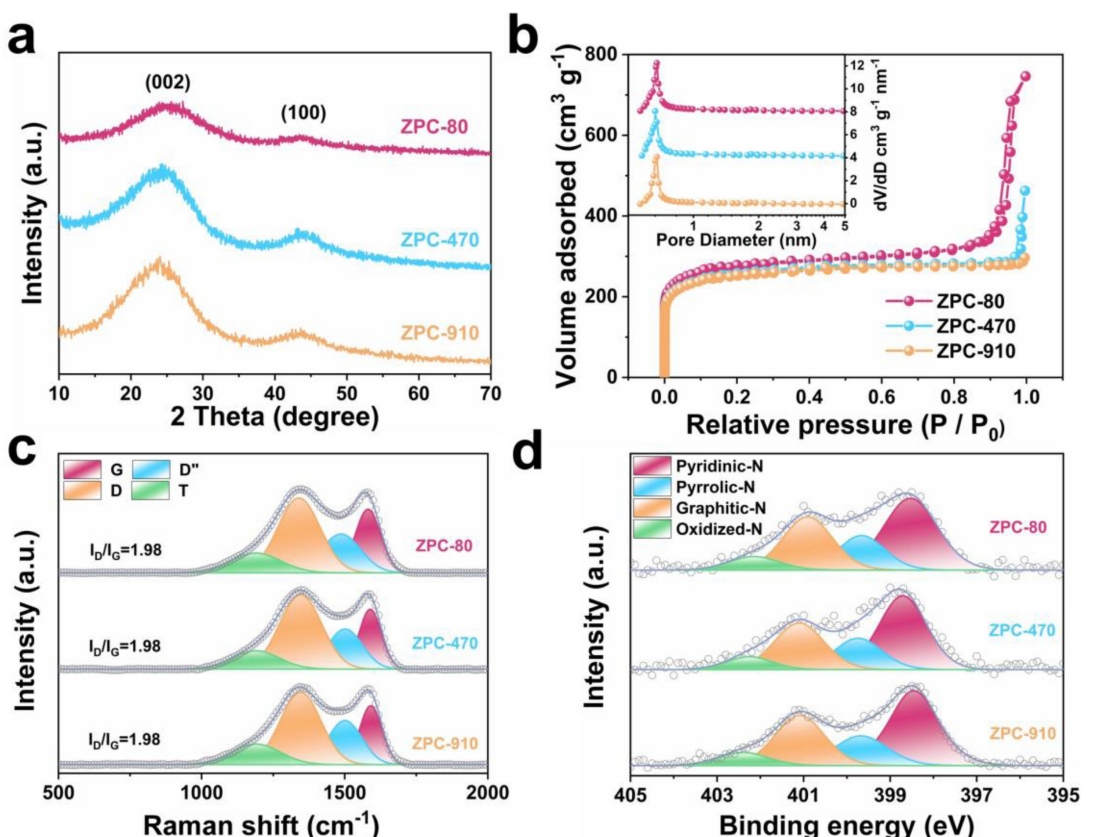


Figure 2. (a) XRD patterns, (b) N_2 adsorption-desorption isotherms, pore size distributions, (c) Raman, and (d) XPS of ZPC-Xs.

pyridinic nitrogen, pyrrolic nitrogen, and graphitic nitrogen, may have different electron affinities and chemical activities, thus they may play different roles in altering the electronic structure and surface properties of porous carbon particles.^[24] To eliminate the influence of nitrogen doping on the study of size effects, we used X-ray photoelectron spectroscopy (XPS) analysis to investigate the nitrogen doping characteristics of the three samples. XPS measurements determined the elemental composition of the samples to include Zn, N, O, and C, consistent with the composition of ZIF-8-derived carbon (Figure S6). High-resolution N 1s spectra revealed the chemical environment of nitrogen doping, showing the presence of pyridinic-N (~398.4 eV), pyrrolic-N (~399.6 eV), graphitic-N (~400.8 eV), and oxidized-N (~402.1 eV) in all three samples (Figure 2d).^[25] By calculating the fitted peak areas, we analyzed the relative content of the four nitrogen species (Figure S7). All three samples exhibit consistent relative contents of pyridinic-N, pyrrolic-N, graphitic-N, and oxidized-N, namely, 44.4%,

18.6%, 29.3%, and 7.7%, respectively. This result lays the foundation for further evaluating the impact of size effects on battery performance.

To delve deeper into the sodium storage behavior of ZPC materials and their relationship with particle size changes, we used metallic sodium foil as the counter electrode and a 1 mol L^{-1} NaClO₄ solution in a blend of ethylene carbonate and dimethyl carbonate (in a 1:1 v/v ratio) as the electrolyte for the assembly of button cells. The electrochemical sodium storage behavior of sodium ions in the 0.01 to 3.0 V voltage range was studied in detail using Cyclic Voltammetry (CV) and constant current charge-discharge tests. The CV curves of ZPC-Xs materials at a scan rate of 0.1 mV s^{-1} , as shown in Figure 3a, display broad peaks below 0.1 V during oxidation, with no sharp peaks, indicating that their sodium storage mechanism is mainly dominated by defect adsorption.^[26] The ZPC-80 electrode exhibits significantly broadened oxidation-reduction peaks above 1.75 V, and as the size increases, the CV curves

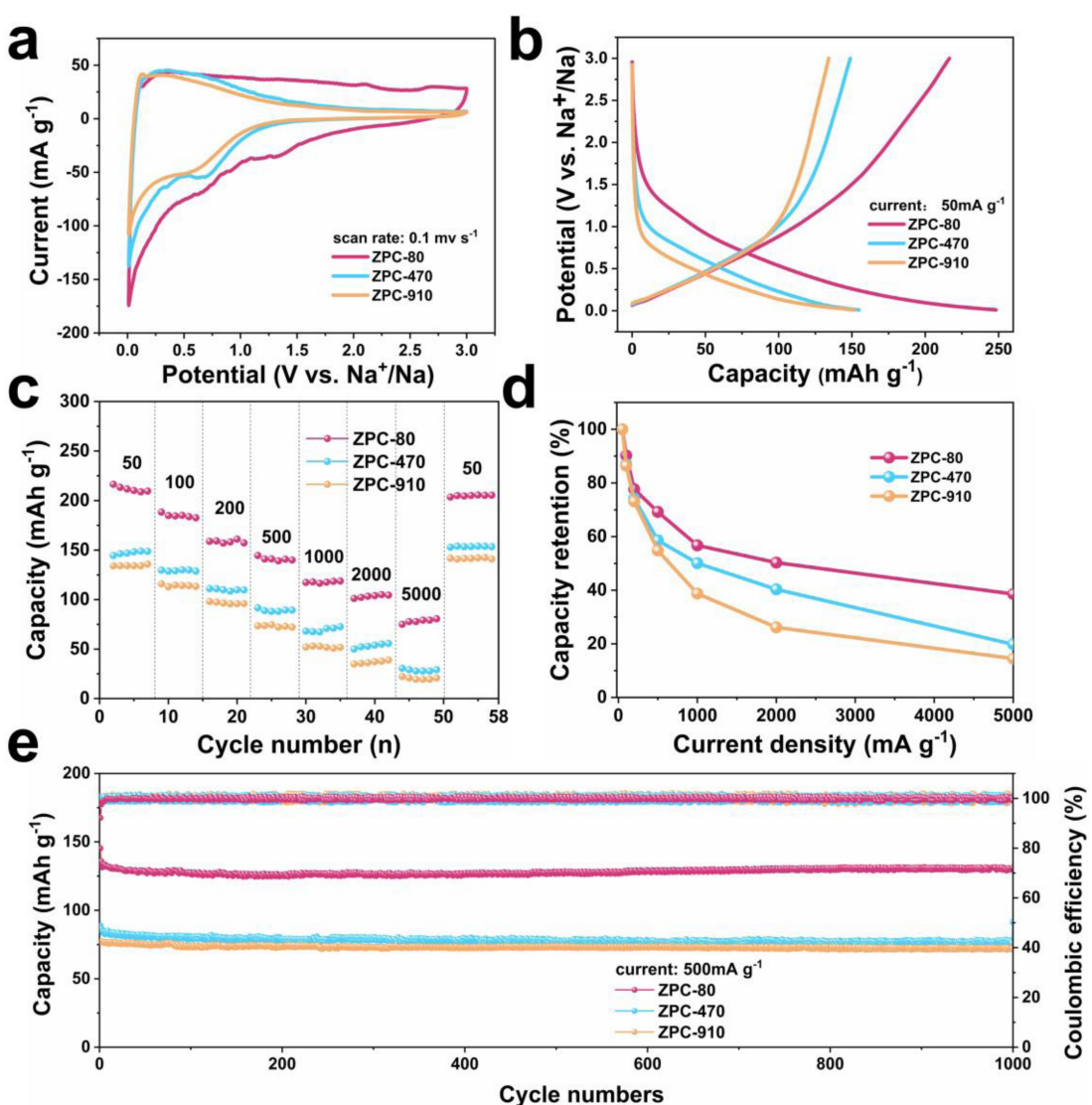


Figure 3. CV curves of ZPC-Xs (a) and galvanostatic charge-discharge (GCD) curves at 50 mA g^{-1} (b). Rate capabilities of ZPC-Xs (c) and their capacity retention (d) at corresponding currents. (e) Long cycling behaviors of ZPC-Xs anode materials were at 500 mA g^{-1} .

gradually narrow, reflecting stronger physical adsorption due to the increased specific surface area.^[27] ZPC-Xs have two distinct reduction peaks at around 0.1 V and 0.7 V. These peaks are typically attributed to the insertion and adsorption of sodium ions within the porous carbon.^[28]

Figure 3b shows galvanostatic charge-discharge tests at 50 mA g⁻¹, where ZPC-Xs exhibit sloping curves without clear plateaus. This indicates that in porous carbon, the storage mechanism of sodium ions primarily involves pseudocapacitive behavior through defect adsorption, independent of the size of nanometer-sized particles, consistent with the CV curve results. The reversible capacities of ZPC-80, ZPC-470, and ZPC-910 are 248.2, 156.7, and 151.7 mAh g⁻¹, respectively. The reversible capacity of ZPC-Xs gradually decreases with increasing particle size. This trend is consistent with the change in BET surface area, suggesting a possible direct correlation between the microstructural changes of electrode materials and electrochemical behavior, which will be discussed in detail later. Figure S8 depicts the first charge-discharge curves and Coulombic efficiency of ZPC-X. It can be observed from the figure that at a current density of 50 mA g⁻¹, the initial charge-discharge efficiency (ICE) of samples ZPC-80, ZPC-470, and ZPC-910 are 26.6%, 26.9%, and 27.0%, respectively. Despite the potentially adverse effects of larger specific surface areas on the ICE performance of porous carbon electrodes, we observe that their ICE performances are quite similar, suggesting that the size differences may not significantly affect ICE.

In order to assess the impact of size effects on battery performance, rate capability, and cycling stability, we conducted tests on ZPC-Xs. The results of rate tests (see Figure 3c, S9–11) reveal that the ZPC-80 electrode exhibits favorable performance across various current densities. At current densities of 50, 100, 200, 500, 1000, and 2000 mA g⁻¹, the ZPC-80 electrode provides reversible capacities of 210.2, 190.1, 158.0, 142.8, 119.5, and 105.4 mAh g⁻¹, respectively. Impressively, even at a high current density of 5000 mA g⁻¹, the ZPC-80 electrode maintains a capacity of 81.4 mAh g⁻¹, achieving a capacity retention rate of 39.1%. Upon returning to a current density of 50 mA g⁻¹, the capacity rebounds to 205.5 mAh g⁻¹, underscoring the significant rate capability of ZPC-80. Furthermore, at low currents, the capacity retention is nearly unaffected by changes in particle size. However, as the current density increases, especially above 500 mA g⁻¹, the disparity in capacity retention between different sizes gradually widens. This is attributed to the reduced particle size, which increases the specific surface area, enhancing the contact surface area between the electrode material and the conductive agent, thus improving the electrode-electrolyte interaction. Nevertheless, as the current further increases, the influence of Ohmic resistance becomes evident, leading to a gradual decrease in capacity retention^[28a, 29].

Figure 3e illustrates the long-term cycling performance of ZPC-Xs within the potential range of 0.01 to 3 V. All samples exhibited excellent stability in the cyclic tests, especially ZPC-80, which retained 97% of its initial capacity after 1000 cycles, while ZPC-470 and ZPC-910 retained 95% and 93% of their initial capacity, respectively. This result is attributed to the

"defect adsorption" as the primary sodium storage mechanism, which did not undergo significant structural changes during the cyclic process. Additionally, the close-to-100% Coulombic efficiency for all samples also demonstrates the key to the efficient pseudocapacitive reaction.

To better understand the precise control of size on specific capacity and reveal the key mechanisms, this paper proposes a mathematical model based on a spherical particle core-shell structure to establish the correlation between size and specific surface area (Figure 4a). Simplifying the ZPC rhombic dodecahedron structure to a sphere (Figure 4c), assuming the internal specific surface area of ZPC is the same ($S_{BET(internal)}$), particle size (d), and ZPC volume density (ρ), Equation 1 is obtained.

$$\begin{aligned} S_{BET} &= S_{BET(external)} + S_{BET(internal)} \\ &= \frac{\pi d^2}{\frac{1}{6}\pi d^3 \rho} + S_{BET(internal)} \\ &= \frac{8146.58}{d} + 948 \end{aligned} \quad (1)$$

The specific capacity is largely constrained by the size-dominated specific surface area of the particles. By combining the results of BET results and charge-discharge curves in the previous sections, we observe that with the increase in particle size, both specific surface area and discharge capacity exhibit a similar decreasing trend. Through a comparative analysis of specific surface area and capacity (Figure 4b), we identify a linear relationship between them, which can be explained by considering multiple factors comprehensively. Firstly, there is a linear relationship between defect concentration and the battery's slope capacity.^[30] Raman spectroscopy analysis confirms that particles of different sizes have similar defect densities. In ZPC, the primary storage mechanism for sodium ions is through defect adsorption on the pseudocapacitive surface. Figure 4d demonstrates that as the particle sizes enlarge, the decrease in specific surface area reduces the effective region of defect adsorption, leading to a decrease in battery capacity. Therefore, the linear relationship between the specific capacity of SIBs and their pseudocapacitance is established. This finding deepens our understanding of the interrelationship between the size characteristics of porous carbon and battery performance.

Apart from the capacity analysis, we conducted an in-depth study of the electrochemical sodium storage mechanism of ZPC-Xs materials to more comprehensively reveal the impact of size effect. The kinetic analysis of the Cyclic Voltammetry (CV) curve has significant value in studying the rate aspects of sodium storage. In this study, CV examinations were carried out at various scan rates ranging from 0.1 to 5.0 mV s⁻¹ (depicted in Figure 5a–c), elucidating the correlation between peak current (i) and scan rate (v). The findings revealed that they adhere to a power function relationship:

$$i = av^b \quad (2)$$

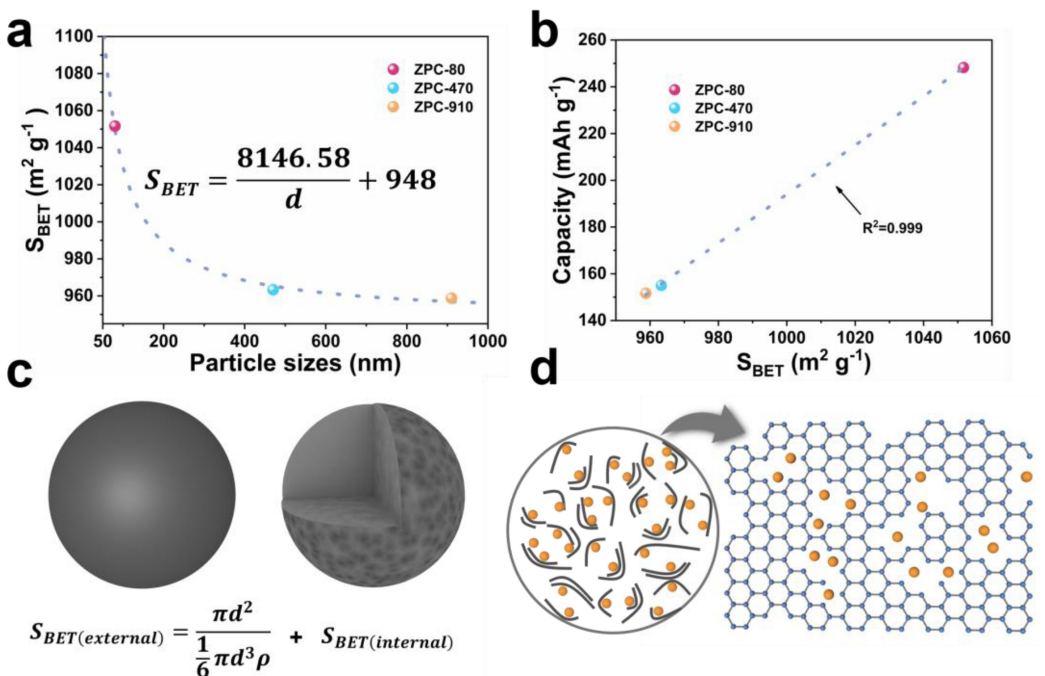


Figure 4. (a), (c) A model fitting the particle sizes, and specific surface area of the ZPC-Xs. (b) presents a linear relationship between discharge specific capacity and specific surface area, (d) storage behavior of sodium ions in ZPC-Xs.

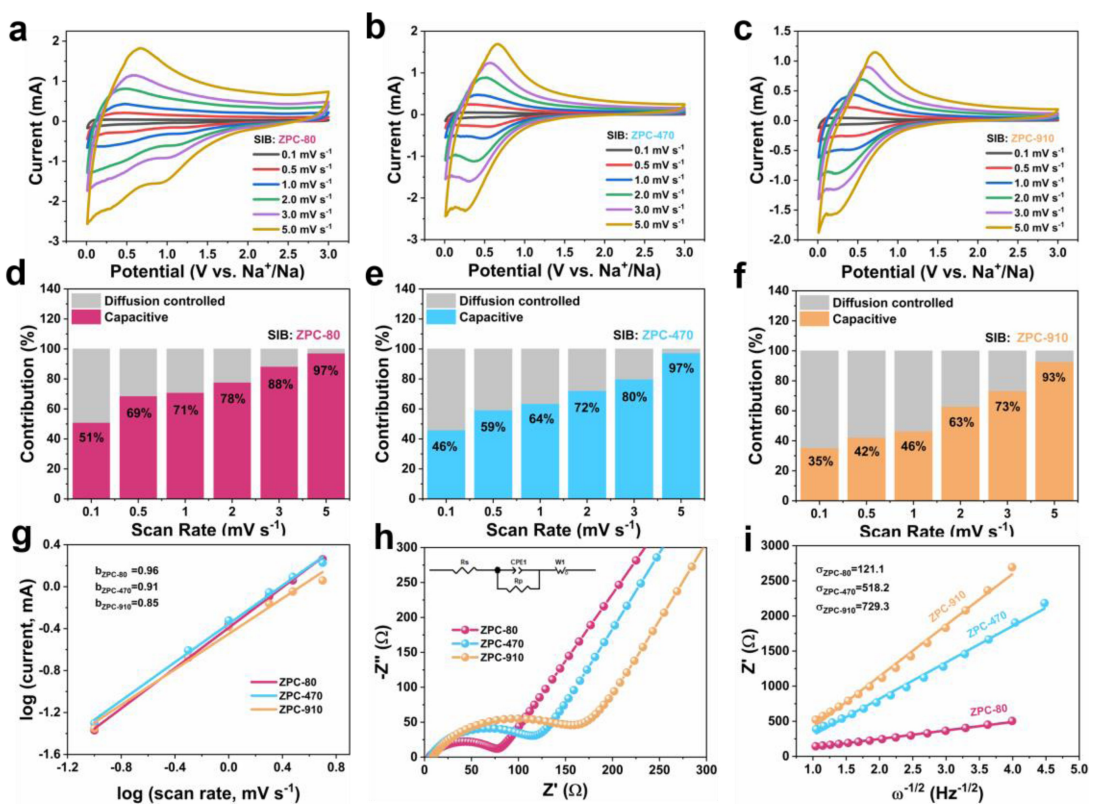


Figure 5. CV curves of (a) ZPC-80, (b) ZPC-470 and (c) ZPC-910 at different scan rates; (d-f) Capacitive contribution ratio of ZPC-Xs under varying scan rates; Fitting plots of ZPC-Xs for (g) the reduction peak. (h) Nyquist plots of ZPC-Xs. (i) Linear fits of Z' versus $\omega^{-0.5}$ in the low-frequency region for ZPC-Xs.

In this context, the determination of the b value can be derived from the gradient of the $\log(i)$ vs. $\log(v)$ plot. This b value serves as a criterion to distinguish whether the electro-

chemical reaction is diffusion-controlled ($b=0.5$) or surface-controlled ($b=1$). For kinetic analysis, the oxidation peak at approximately 0.01 V (peak 1) and the reduction peak at around

0.5 V (peak 2) were chosen. Both $\log(I_{p1})$ and $\log(I_{p2})$ show a linear relationship with $\log(v)$ (Figure 5g and S12–14). In ZPC-Xs samples, all b values are close to 1, especially for ZPC-80 at the oxidation peak, with a b value of 0.96, higher than that of ZPC-470 and ZPC-910 (0.91 and 0.85, respectively), indicating that the electrochemical behavior in the sodium storage process is almost entirely controlled by surface capacitance, with smaller particle sizes being more prominent in this capacitance-controlled process.^[26]

On this basis, we estimate the contributions of diffusion-controlled and capacitance-related processes using the following formula:

$$i(V) = k_1 v + k_2 v^{1/2} \quad (3)$$

Here, $k_1 v$ and $k_2 v^{1/2}$ denote the energy storage contributions corresponding to the capacitance-controlled and diffusion-controlled processes, respectively.^[31] As depicted in Figure 5d–f, CV curve analysis indicates that the surface control reaction tends to increase with the scanning rate. At high scan rates, the electrochemical behavior of ZPC-Xs materials is mainly contributed by pseudocapacitive behavior, especially at 5 mV s⁻¹, where the capacity contribution reaches 97%. Additionally, Figure S15–17 shows the typical CV curves of ZPC-Xs at 1.0 mV s⁻¹, indicating that pseudocapacitive behavior (colored filled areas) contributes 71%, 64%, and 46% to the total electrochemical reaction, respectively. By comparing the detailed area distributions of different materials, the differences in the sloping capacity storage process among the three materials can be clearly observed. Therefore, a reduction in size mainly plays a role in enhancing physical adsorption above 1.75 V in the high-potential area and enhancing surface capacitive response in the mid-to-high potential area between 0.1–0.75 V, further confirming the contribution of surface capacitance of nanoporous carbon to the sloping capacity.

To comprehensively understand the electrochemical reaction kinetics of ZPC-Xs materials, we performed Electrochemical Impedance Spectroscopy (EIS) analysis in the charged state after the first cycle. The fitting results using an equivalent circuit model showed that all ZPC-Xs samples exhibit capacitive-like curves, attributed to the high porosity of the nano-porous carbon network, providing abundant surface area for charge adsorption. The Ohmic resistance (R_s), mainly constituted by the electrolyte resistance and the contact resistance between the electrode and the current collector, is represented in the Nyquist plot by the intersection on the real impedance axis at high frequencies (Figure S18). The lower R_s value of ZPC-80 indicates its superior electronic conductivity compared to larger-sized samples, possibly due to the contact area between the electrode material and conductive agent determining the intrinsic conductivity. The smaller size of ZPC-80 results in a larger contact area with the conductive agent, thereby leading to a lower R_s value.^[8a] In the mid-to-high frequency range, the charge transfer resistance (R_{ct}) can be clearly defined corresponding to the related semicircle (Figure 5h), with ZPC-80's R_{ct} being only 76 Ω, significantly lower than ZPC-470 (111 Ω) and ZPC-910 (158 Ω), indicating that size reduction is beneficial for

charge transfer, thereby enhancing the electrochemical performance.^[32]

Additionally, we calculated the diffusion coefficient (D) of sodium ions to further understand the kinetic properties of the material. The diffusion coefficient is determined utilizing the following formula:

$$D = \frac{R^2 T^2}{2A^2 n^4 F^4 C^2 \sigma^2} \quad (4)$$

where R, T, A denote the gas constant, absolute temperature, and electrode surface area, respectively; n and F represent the number of electrons transferred per molecule and the Faraday constant, respectively; C is the molar concentration of sodium ions; σ is the slope of the Nyquist plot. By fitting Z' and $\omega^{-1/2}$, as shown in Figure 5i, we calculated the diffusion coefficient of ZPC-80 to be 6.86×10^{-13} cm²s⁻¹, far higher than ZPC-470 (3.7×10^{-14} cm²s⁻¹) and ZPC-910 (1.8×10^{-14} cm²s⁻¹). This finding further corroborates the outstanding diffusion performance of the ZPC-80 material. However, the ion diffusion coefficients calculated using GITT (Galvanostatic Intermittent Titration Technique) exhibit an opposite trend to the results obtained from EIS,^[33] as shown in Figure S19. This discrepancy may arise from the fact that the diffusion coefficients derived from EIS analysis are based on impedance behavior, which may reflect diffusion processes occurring at different time scales. Interfaces tend to reduce impedance, thus favoring the performance of ZPC-80. On the other hand, GITT involves intermittent current pulses and relaxation periods, providing diffusion kinetic information at specific time intervals. The presence of interfaces may impede ion diffusion.

3. Conclusions

This study systematically analyzes the impact of ZPC with different particle sizes, derived from ZIF-8, on the negative electrode of SIBs. The storage mechanism of sodium ions in ZPC primarily revolves around defect adsorption. In SIBs, the specific capacity is closely related to the changes in specific surface area caused by particle size. Through mathematical modeling and electrochemical dynamics analysis, we delve into the mechanisms of size effects on battery performance, revealing a linear relationship between specific capacity and specific surface area. Size reduction enhances physical adsorption and surface capacitance response. ZPC-80 exhibits lower resistance and higher diffusion coefficient, indicating that size reduction improves electronic conductivity and charge transfer efficiency, achieving excellent rate performance and cycle stability. Our work not only advances the theoretical understanding of porous carbon electrode performance but also offers practical guidance for the further application of nano-porous carbon in the realm of energy storage, providing new ideas and strategies for battery technology development.

Conflict of Interests

The authors declare no conflict of interest.

Data Availability Statement

The data that support the findings of this study are available from the corresponding author upon reasonable request.

Keywords: ZIF-8 Derived Porous Carbon (ZPC) • High-rate • defect adsorption • Sodium-ion batteries

- [1] a) Y. Huang, X. Zhong, X. Hu, Y. Li, K. Wang, H. Tu, W. Deng, G. Zou, H. Hou, X. Ji, *Adv. Funct. Mater.* **2023**, 34(4), 2308392; b) N. LeGe, X.-X. He, Y.-X. Wang, Y. Lei, Y.-X. Yang, J.-T. Xu, M. Liu, X. Wu, W.-H. Lai, S.-L. Chou, *Energy Environ. Sci.* **2023**, 16(12), 5688–720; c) A. Chojnacka, X. Pan, C. Bachetzky, E. Brunner, F. Béguin, *Energy Storage Mater.* **2022**, 51, 719;
- [d) Y. Xi, X. Wang, H. Wang, M. Wang, G. Wang, J. Peng, N. Hou, X. Huang, Y. Cao, Z. Yang, D. Liu, X. Pu, G. Cao, R. Duan, W. Li, J. Wang, K. Zhang, K. Xu, J. Zhang, X. Li, *Adv. Funct. Mater.* **2024**, 34(16), 2309701.
- [2] D. Cheng, Z. Li, M. Zhang, Z. Duan, J. Wang, C. Wang, *ACS Nano* **2023**, 17, 19063.
- [3] S. Qiao, Q. Zhou, M. Ma, H. K. Liu, S. X. Dou, S. Chong, *ACS Nano* **2023**, 17, 11220.
- [4] X. Chen, N. Sawut, K. Chen, H. Li, J. Zhang, Z. Wang, M. Yang, G. Tang, X. Ai, H. Yang, Y. Fang, Y. Cao, *Energy Environ. Sci.* **2023**, 16, 4041.
- [5] G. M. Tomboc, Y. Wang, H. Wang, J. Li, K. Lee, *Energy Storage Mater.* **2021**, 39, 21.
- [6] a) Y. Wang, H. Dong, N. Katyal, B. S. Vishnugopi, M. K. Singh, H. Hao, Y. Liu, P. Liu, P. P. Mukherjee, G. Henkelman, J. Watt, D. Mitlin, *Adv. Energy Mater.* **2023**, 13, 2204402; b) W. Liu, H. Zhi, X. Yu, *Energy Storage Mater.* **2019**, 16, 290.
- [7] W. Ma, G. Huang, L. Yu, X. Miao, X. An, J. Zhang, Q. Kong, Q. Wang, W. Yao, *J. Colloid Interface Sci.* **2024**, 654, 1447–1457.
- [8] a) P. Geng, L. Wang, M. Du, Y. Bai, W. Li, Y. Liu, S. Chen, P. Braunstein, Q. Xu, H. Pang, *Adv. Mater.* **2022**, 34, e2107836; b) Z. Tang, R. Zhang, H. Wang, S. Zhou, Z. Pan, Y. Huang, D. Sun, Y. Tang, X. Ji, K. Amine, M. Shao, *Nat. Commun.* **2023**, 14, 6024.
- [9] J. Li, X. Chang, T. Huang, B. Wang, H. Zheng, Q. Luo, D.-L. Peng, Q. Wei, *Energy Storage Mater.* **2023**, 54, 724.
- [10] Q. Wei, X. Chang, D. Butts, R. DeBlock, K. Lan, J. Li, D. Chao, D.-L. Peng, B. Dunn, *Nat. Commun.* **2023**, 14, 7.
- [11] J. M. Fan, J. J. Chen, Q. Zhang, B. B. Chen, J. Zang, M. S. Zheng, Q. F. Dong, *ChemSusChem* **2015**, 8, 1856.
- [12] Q. He, X. Jin, Z. Li, Z. Cai, J. Tian, J. Hui, H. Zhang, *ACS Appl. Mater. Interfaces* **2021**, 14, 1203.
- [13] J. Li, D. Yan, X. Zhang, S. Hou, T. Lu, Y. Yao, L. Pan, J. Mater. Chem. A **2017**, 5, 20428.
- [14] X. Xie, K. Huang, X. Wu, N. Wu, Y. Xu, S. Zhang, C. Zhang, *Carbon* **2020**, 169, 1.
- [15] J. Troyano, A. Carne-Sanchez, C. Avci, I. Imaz, D. MasPOCH, *Chem. Soc. Rev.* **2019**, 48, 5534.
- [16] Y. Zhang, Y. Jia, M. Li, L. Hou, *Sci. Rep.* **2018**, 8, 9597.
- [17] H. H. Yeung, A. F. Sapnik, F. Massingberd-Mundy, M. W. Gaulois, Y. Wu, D. A. X. Fraser, S. Henke, R. Pallach, N. Heidenreich, O. V. Magdysyuk, N. T. Vo, A. L. Goodwin, *Angew. Chem. Int. Ed. Engl.* **2019**, 58, 566.
- [18] P. Lu, Y. Sun, H. Xiang, X. Liang, Y. Yu, *Adv. Energy Mater.* **2018**, 8(8), 1702434.
- [19] a) T. Zhao, Y. Wei, J. Wang, Q. Wang, Y. Chen, X. Liu, Y. Zhao, *Sep. Purif. Technol.* **2023**, 317, 123762; b) D. Guo, Y. Fu, F. Bu, H. Liang, L. Duan, Z. Zhao, C. Wang, A. M. El-Toni, W. Li, D. Zhao, *Small Methods* **2021**, 5, 2001137.
- [20] J. Yang, X. Wang, W. Dai, X. Lian, X. Cui, W. Zhang, K. Zhang, M. Lin, R. Zou, K. P. Loh, Q.-H. Yang, W. Chen, *Nano-Micro Lett.* **2021**, 13, 1.
- [21] Y. Dong, S. Zhang, X. Du, S. Hong, S. Zhao, Y. Chen, X. Chen, H. Song, *Adv. Funct. Mater.* **2019**, 29, 1901127.
- [22] Y. Yang, D. Chen, H. Wang, P. Ye, Z. Ping, J. Ning, Y. Zhong, Y. Hu, *Chem. Eng. J.* **2022**, 431, 133250.
- [23] Y. M. Jung, J. H. Choi, D. W. Kim, J. K. Kang, *Adv. Sci.* **2023**, 10(24), 2301160.
- [24] D. Yu, A. Kumar, T. A. Nguyen, M. T. Nazir, G. Yasin, *ACS Sustainable Chem. Eng.* **2020**, 8, 13769.
- [25] a) N. Ahmad, N. Muhammad, H. Chen, J. Wang, C. Wei, M. Khan, R. Yang, *J. Colloid Interface Sci.* **2023**, 650, 1725; b) W. Nie, H. Cheng, X. Liu, Q. Sun, F. Tian, W. Yao, S. Liang, X. Lu, J. Zhou, *J. Power Sources* **2022**, 522, 230994.
- [26] N. Sun, Z. Guan, Yuwen, Y. Cao, Q. Zhu, H. Liu, Z. Wang, P. Zhang, B. Xu, *Adv. Energy Mater.* **2019**, 9, 1901351.
- [27] G. Yang, X. Li, Z. Guan, Y. Tong, B. Xu, X. Wang, Z. Wang, L. Chen, *Nano Lett.* **2020**, 20, 3836.
- [28] a) L. Liu, Y. He, S. Yin, X. Chang, J. Zhang, L. Peng, J. Li, Y. Ma, Q. Wei, K. Lan, D. Zhao, *Mater.* **2023**, 6, 3099; b) M. Liu, F. Wu, Y. Gong, Y. Li, Y. Li, X. Feng, Q. Li, C. Wu, Y. Bai, *Adv. Mater.* **2023**, 35, 2300002; c) J. Yan, H. Li, K. Wang, Q. Jin, C. Lai, R. Wang, S. Cao, J. Han, Z. Zhang, J. Su, K. Jiang, *Adv. Energy Mater.* **2021**, 11, 2003911.
- [29] Z. Zhang, R. Wang, J. Zeng, K. Shi, C. Zhu, X. Yan, *Adv. Funct. Mater.* **2021**, 31, 2106047.
- [30] C. Bommier, T. W. Surta, M. Dolgos, X. Ji, *Nano Lett.* **2015**, 15, 5888.
- [31] T. Bashir, S. Zhou, S. Yang, S. A. Ismail, T. Ali, H. Wang, J. Zhao, L. Gao, *Electrochim. Energy Rev.* **2023**, 6(1), 5.
- [32] Y. Zhao, Z. Hu, C. Fan, P. Gao, R. Zhang, Z. Liu, J. Liu, J. Liu, *Small* **2023**, 19, 2303296.
- [33] X. Song, X. Li, H. Shan, J. Wang, W. Li, K. Xu, K. Zhang, H. M. K. Sari, L. Lei, W. Xiao, J. Qin, C. Xie, X. Sun, *Adv. Funct. Mater.* **2024**, 34(5), 2303211.

Manuscript received: February 28, 2024

Revised manuscript received: April 10, 2024

Accepted manuscript online: April 15, 2024

Version of record online: May 17, 2024